Controlling radial fingering patterns in miscible confined flows

Ching-Yao Chen,* C.-W. Huang, and L.-C. Wang
Department of Mechanical Engineering, National Chiao Tung University, Hsinchu, Taiwan, Republic of China

José A. Miranda†
Departamento de Física, Universidade Federal de Pernambuco, Recife, PE 50670-901, Brazil
(Received 8 September 2010; published 11 November 2010)

Injection-driven immiscible flow in radial Hele-Shaw cells results in highly ramified patterns if the injection rate is constant in time. Likewise, time-dependent gap immiscible flow in lifting Hele-Shaw cells leads to intricate morphologies if the cell's gap width grows exponentially with time. Recent studies show that the rising of these complex fingered structures can be controlled by properly adjusting the injection rate, and the time-dependent gap width. We investigate the effectiveness of these control strategies assuming that the fluids involved are miscible. Despite the absence of surface tension effects, intensive numerical simulations support the stabilizing role of these controlling protocols. Splitting, merging and competition of fingers are all inhibited. The sensitivity of the system to changes in the initial conditions and Péclet numbers is also discussed.

DOI: 10.1103/PhysRevE.82.056308 PACS number(s): 47.15.gp, 47.20.Hw, 47.54.−r, 47.51.+a

I. INTRODUCTION

During several decades the Saffman-Taylor instability [1,2] has been serving as a paradigm of interfacial pattern formation systems, both as a relatively simple example of morphological instability, and as a nontrivial but solvable problem of pattern selection. It arises at the interface separating two viscous fluids constrained to flow in the narrow gap between closely-spaced parallel plates of a Hele-Shaw cell. Under constant injection radial flow rate [3] the most typical signature of such an instability is the occurrence of fingerlike structures which split at their tips, leading to the emergence of a convoluted dense-branching morphology. Over the years this constant injection rate radial viscous fingering problem has been extensively studied both experimentally [4–6] and theoretically [7–11].

An interesting variation of the classic radial flow Saffman-Taylor situation also results in the formation of complex structures: it is the so-called lifting radial Hele-Shaw flow [12–15]. In this lifting version of the problem, the more viscous fluid is placed at the center of a Hele-Shaw cell, surrounded by a less viscous fluid, and the upper cell plate is moved upwards. While the more viscous fluid is stretched vertically along the variable gap direction, the fluid-fluid interface moves inwards allowing the penetration of multiple fingers of the outer, less viscous fluid. This viscosity-driven unstable scenario culminates in the rising of visually striking fingering patterns. However, in contrast to the constant injection radial flow where finger tip-splitting abounds, the most noteworthy interfacial feature in conventional time-dependent gap lifting Hele-Shaw flows is the strong competition among the penetrating fingers. By "conventional" we mean those usual setups studied in both theory and experiments, in which the cell gap width grows linearly or exponentially with time [12–15].

Despite the richness and beauty of the radial patterns produced by constant injection and conventional lifting, in many practical circumstances such as in oil recovery [16] and adhesion science applications [17] the formation of convoluted interfacial shapes is quite undesirable. For instance, the Saffman-Taylor instability is a major contributor for poor oil recovery processes, once rapidly evolving branched fingers of water reach the entrance of the well, so that mainly water, and not the more viscous petroleum is retrieved. Moreover, the growing of intricate patterns due to lifting is a critical impediment when mechanical, nondestructive removal of adhered surfaces is needed. These two illustrative situations exemplify the importance of achieving improved control of the shape of emergent patterns, and try to enhance the efficiency of the various physical and engineering processes related to viscous fingering phenomena.

Very recent investigations have tackled the problem of controlling viscous fingering in radial Hele-Shaw flows with *immiscible* fluids [18–20]. With regards to the injection-driven situation, meticulous experiments, analytical calculations, and sophisticated numerical simulations have shown that the development of the usual multibranched morphology could be constrained by properly choosing the time dependence of the injection flux. Instead of employing a constant pumping routine, they assumed a variant injection rate which scaled with time like $t^{-1/3}$. Under such circumstances, the traditional ramified patterns are indeed suppressed, and replaced by symmetric shapes containing a prescribed number of fingers. This behavior is quite robust and independent of the initial perturbation conditions. With respect to the lifting flow case, the conventional linear or exponential time dependencies have been substituted by a variant gap width which scales with time with exponent $-2/7$ [20]. For this particular situation, it has been shown that finger competition is restrained leading to a more ordered array of fingers. As pointed out earlier, these suggestive controlling mechanisms have been tested for *immiscible* displacements, where surface tension plays a key role in both stabilization protocols.

Motivated by the stimulating results obtained in Refs. [18–20] we examine similar situations, but now considering

*chingyao@mail.nctu.edu.tw
†jme@df.ufpe.br

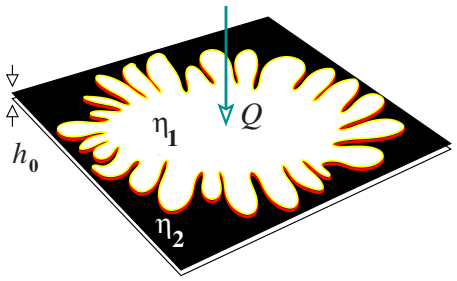

FIG. 1. (Color online) Schematic setup for the injection-driven radial Hele- Shaw flow with miscible fluids. The constant cell gap width is denoted by h_0, and the less viscous fluid 1 is injected into the more viscous fluid 2. The injection rate Q can be either constant or time-varying.

that the fluids involved are *miscible*. Miscible displacements are characterized by negligible surface tension, so that the interplay of diffusive, convective, and viscous effects dictate the pattern formation behavior. We have already carried out highly accurate numerical simulations for miscible radial Hele-Shaw flow under constant injection rate [11] and conventional lifting [14] conditions. We have verified that typically miscible patterns are even more irregular and complex than their immiscible counterparts. Therefore, the search for control mechanisms in confined miscible fluids is certainly a challenging topic. In this work we revisit the miscible injection and lifting problems in radial Hele-Shaw geometry, but now focus on analyzing how the stabilizing procedures introduced in [18–20] could influence the ultimate appearance of the fluid-fluid diffusive interface.

II. INJECTION-DRIVEN MISCIBLE HELE-SHAW FLOW

A. Governing equations

Consider a Hele-Shaw cell of constant gap thickness h_0 containing two miscible, incompressible, viscous fluids (Fig. 1). Denote the viscosities of the fluids as η_1 and η_2, and assume that $\eta_2 > \eta_1$. Fluid 1 is injected into fluid 2 at a given injection rate Q (equal to the area covered per unit time) which may depend on time. The dimensionless equations governing the dynamical evolution of the system are the traditional gap averaged Hele-Shaw flow equations [11].

$$\nabla \cdot \mathbf{u} = 0, \tag{1}$$

$$\nabla p = -\eta \mathbf{u}, \tag{2}$$

$$\frac{\partial c}{\partial t} + \mathbf{u} \cdot \nabla c = \frac{1}{\mathrm{Pe}} \nabla^2 c. \tag{3}$$

Equation (1) expresses the incompressibility condition, where $\mathbf{u}$ denotes the two-dimensional (2D) gap averaged velocity. Darcy's law is expressed by Eq. (2) where p is a scaled hydrodynamic pressure. The gap averaged concentration equation is given by Eq. (3), where the concentration of the fluid 1 is represented by c, and

$$\mathrm{Pe} = \frac{Q_c}{2\pi D} \tag{4}$$

is a Péclet number which is a measure of the relative importance of advection to diffusion. For the miscible flow situations studied in this work, we focus on diffusive effects rather than on surface tension, so that in some sense the Péclet number replaces the usual capillary number (ratio of viscous to surface tension effects) [18–20]. Q_c denotes a *constant* injection rate, and D is the constant diffusion coefficient. The dimensionless viscosity of the mixture is assumed to vary exponentially with concentration

$$\eta(c) = \exp[(\mathcal{R}(1-c)], \tag{5}$$

with $\mathcal{R} = \ln(\eta_2/\eta_1)$ representing a viscosity parameter which is related to the viscosity contrast $\mathcal{A} = (e^{\mathcal{R}} - 1)/(e^{\mathcal{R}} + 1)$. The specific functional form relating viscosity and concentration in Eq. (5) has been originally proposed some time ago in a seminal paper by Tan and Homsy [21]. We stress that the validity and suitability of Eq. (5) has been demonstrated by contrasting numerical simulations [22,23] and experiments [24–26] for various combinations of fluids. We point out that the less viscous fluid (fluid 1) always serves as the displacing fluid in both the injection and lifting cases. The concentration of the less viscous fluid 1 is denoted by c, so that $c=1$ ($c=0$) represents a pure fluid 1 (2).

As in Ref. [11] the expressions presented above have been made dimensionless by taking an arbitrary length ℓ as the characteristic length scale. In conjunction with the source strength Q_c, we then obtain a time scale as $2\pi\ell^2/Q_c$, a velocity scale in the form of $Q_c/2\pi\ell$, and a characteristic pressure $6\eta_1 Q_c/\pi h_0^2$. Viscosity is rescaled by η_1.

In order to solve the governing Eqs. (1)–(3) numerically, we recast them into the well known stream function-vorticity formulation (ϕ, ω) [23]. By employing such an approach we rewrite the gap averaged velocity in Eq. (2) as $\mathbf{u} = \mathbf{u}_r + \mathbf{u}_{pot}$, where $\mathbf{u}_r$ is the rotational component of the velocity, and $\mathbf{u}_{pot}$ represents its potential component. Likewise, we define the total stream function of the system as $\phi_0 = \phi + \phi_{pot}$, where ϕ and ϕ_{pot} denote the rotational and potential stream functions, respectively. Since $\nabla^2 \phi_{pot} = 0$, we end up with the equations

$$u_r = \frac{\partial \phi}{\partial y}, \quad v_r = -\frac{\partial \phi}{\partial x}, \tag{6}$$

$$\nabla^2 \phi = -\omega,$$

$$\omega = -\mathcal{R}\left[u\frac{\partial c}{\partial y} - v\frac{\partial c}{\partial x}\right], \tag{7}$$

where u and v are the components of the velocity vector $\mathbf{u}$ along the x and y directions. Notice that the velocities in Eq. (6) refer to the x-y components of the rotational velocity (u_r, v_r). The numerical scheme we use is based on a combination of spectral methods and compact finite differences. Much more details about these particular numerical methods can be found in specialized books on the subject [27,28]. Extensive discussions about the implementation and valida-

tion of the numerical scheme have been provided in our previous works [11,14].

Our main goal is to contrast the behavior of the emerging miscible patterns obtained under constant injection rate Q_c with those in which a variant time-dependent injection rate $Q(t) \sim t^{-1/3}$ is employed. In both situations the rotational part of the velocity is smooth and can be obtained with high accuracy, while the potential part induced by injection is related to a flow singularity at a source located at the origin making accurate computations more difficult near these locations. To avoid numerical instabilities near $r=0$ we smooth out the point source by distributing its strength in a Gaussian way over a small circular core region. To accomplish this, we consider a "Gaussian source" [29] which is characterized by a core size $\sigma=0.075$. In addition, the initial condition is assumed as an initial fluid core of radius of $r_i=0.1$.

Under the circumstances of *constant* injection rate, the dimensional injected area at a given time can be written as $A_c=Q_c t$. In this case, the dimensionless potential radial velocity satisfying these requirements can be expressed as

$$\mathbf{u}_{pot} = \frac{1}{r}[1 - \exp(-r^2/\sigma^2)]\hat{\mathbf{r}}, \tag{8}$$

where $\hat{\mathbf{r}}$ denotes the unit vector along the radial direction.

Inspired by the results of Refs. [18–20], we consider a time-dependent, variant dimensional injection rate of the form

$$Q(t) = \frac{Q_v}{(1+\alpha t)^{1/3}}, \tag{9}$$

where α is a control parameter with an inverse dimension of time. The corresponding dimensional injected area takes the form $A_v=(3Q_v/2\alpha)[(1+\alpha t)^{2/3}-1]$. Therefore, the dimensionless potential velocity field associated to this *variant* injection case is

$$\mathbf{u}_{pot} = \frac{I}{(1+\beta t)^{1/3} r}[1 - \exp(-r^2/\sigma^2)]\hat{\mathbf{r}}, \tag{10}$$

where $\beta \equiv 2\pi\alpha\ell^2/Q_c$ and $I=Q_v/Q_c$ are two additional dimensionless control parameters.

B. Constant and variant injection scenarios: Numerical results

In this section we present a series of numerical simulations which confront the miscible pattern morphologies under constant and variant injection rates. In order to compare the different patterns under equivalent conditions we focus on the "efficiency" of the injection processes. In other words, we compare situations in which the patterns for constant and variant injection have reached equal area at equal times, i.e., $A_c=A_v=A$ at $t=\tau$ (dimensional conditions taken). In this context, the ratio of injection strengths is readily obtained

$$I = \frac{Q_v}{Q_c} = \frac{2\alpha t}{3[(1+\alpha t)^{2/3} - 1]}. \tag{11}$$

Without loss of generality, for the illustrative simulations shown in this section we consider the representative values $\alpha=1$, $\tau=0.2$, so that $I=1.032$. In addition, we take the parameter $\beta=200$, the viscosity contrast $\mathcal{A}=0.905$, and the Péclet number Pe=600. Here and in Sec. III B we use the largest value of $\mathcal{A}$ for which our numerical code remains stable. For this value of $\mathcal{A}$ the most unstable attainable situation is reached, so that our results can only improve if smaller values of $\mathcal{A}>0$ are used. In the injection-driven simulations a square computational domain with width of two characteristic lengths is chosen, so that $-1 \le x \le +1$ and $-1 \le y \le +1$, and the boundary conditions are prescribed as

$$x = \pm 1 : \phi = 0, \frac{\partial c}{\partial x} = 0, \tag{12}$$

$$y = \pm 1 : \phi = 0, \frac{\partial c}{\partial y} = 0. \tag{13}$$

We begin by analyzing Fig. 2 which depicts the concentration images obtained for increasingly larger values of the dimensionless injected areas $A/\pi=0.1$, 0.2 and 0.4, both for the constant (top row) and variant (bottom row) injection situations. This is done for a given set initial random perturbations (perturbation set 1). When injection is constant in time, typical miscible viscous fingering patterns arise as the mixing front evolves, where initially thin fingers tend to get a little wider. This induces a process in which fingers simultaneously split and merge, creating a significantly convoluted morphology. However, a different kind of pattern forming structure is observed under the variant injection condition. The width of the fingers is more uniform, and finger interpenetration and splitting are unfavored. Consequently, a somewhat more symmetric pattern is obtained, in which the number of resulting fingers (in this case 17) tends to remain basically unaltered as the area is changed. So, despite of the absence of interfacial tension a more regular array of fingers is produced if the variant injection protocol is employed. It should be noted that this stabilizing behavior is not a peculiarity of the particular value of Péclet number we have used (Pe=600). In fact, we have performed a number of additional simulations for the variant injection in a wide range of Péclet numbers ($200 \le \mathrm{Pe} \le 1200$), and always get a regular distribution of fingers whose numbers for $A/\pi=0.4$ vary only from 15 to 21.

We proceed by investigating the robustness of the controlling procedure for variant injection rate $Q(t) \sim t^{-1/3}$ illustrated in Fig. 2. In order to do that, as in Ref. [18] we examine how the overall shapes of the resulting patterns obtained in Fig. 2 behave if we consider different initial conditions. This is done in Fig. 3 which depicts the constant and variant injection patterns for $A/\pi=0.4$, and two distinct sets of initial random perturbations: perturbation set 2 (first column), and perturbation set 3 (second column). It is evident that, though the shapes illustrated in Figs. 2 and 3 for $A=0.4\pi$ are not exactly the same, they are very similar. In particular, the stabilizing mechanism due to variant injection and the total number of resulting fingers are not affected, regardless the change in initial conditions. Interestingly enough, the variant injection miscible patterns shown in Figs. 2 and 3 present some resemblance with equivalent immiscible patterns obtained experimentally in Ref. [19] [see their Fig. 1(d)].

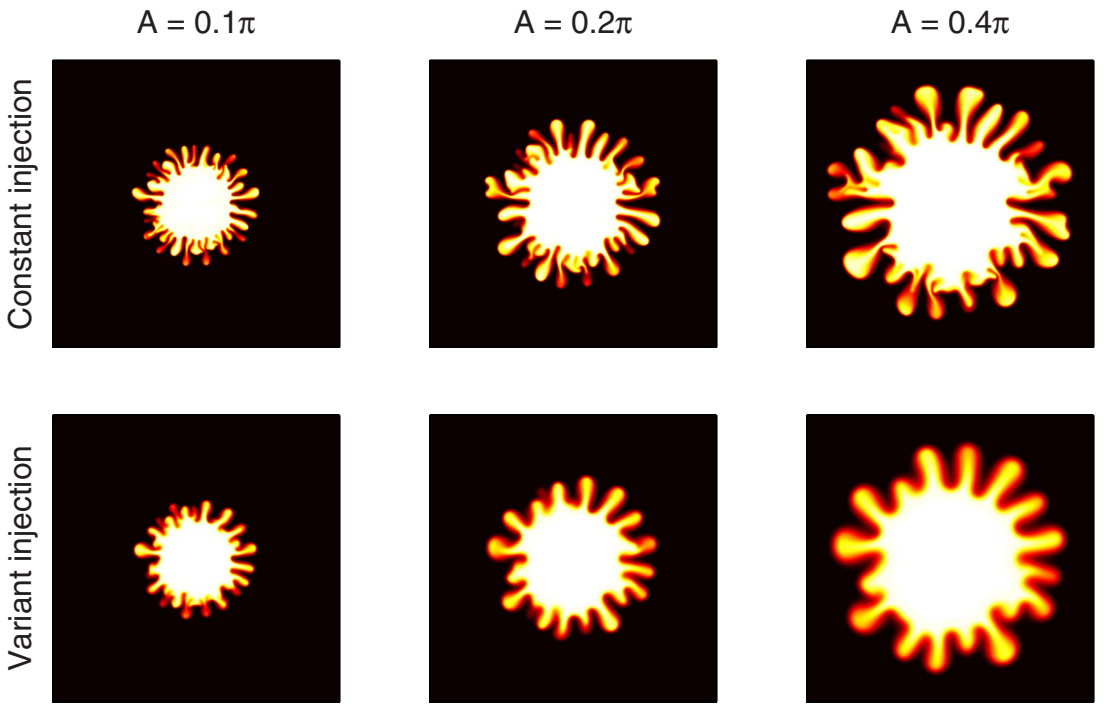

FIG. 2. (Color online) Concentration images for the dimensionless injecting areas A/π=0.1, 0.2 and 0.4, for the cases of constant injection (top row), and variant injection (bottom row).

An alternative and more quantitative account of the role played by the change in the initial conditions in determining the behavior of the evolving mixing interface is offered by the growth of a characteristic quantity related to the perimeter of the mixing boundary region. Unlike the situations involving immiscible fluids, the mixing region between two miscible fluids is not a well defined, sharp interface, but rather a diffuse layer. Nevertheless, in the region of significant concentration gradient, a rescaled mixing interfacial length can be well represented as [23]

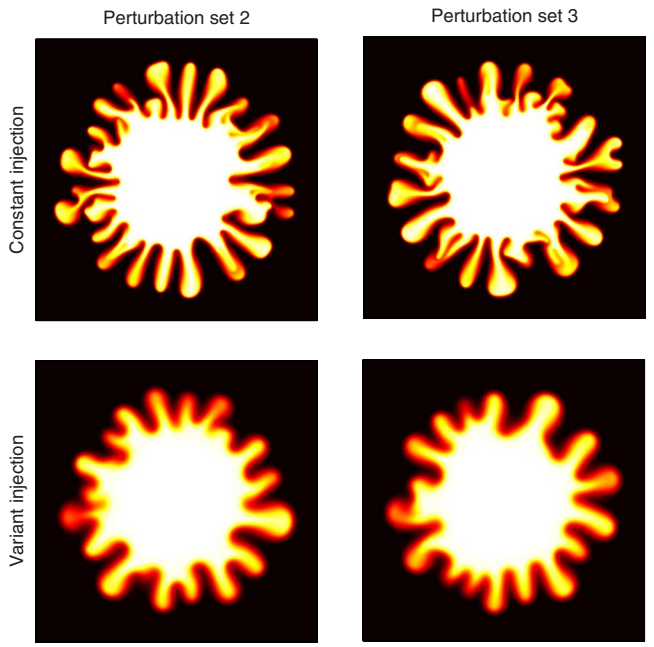

FIG. 3. (Color online) Concentration images for the dimensionless injecting area $A=0.4\pi$ for the cases of constant injection (top row), and variant injection (bottom row). These simulations used the same physical parameters utilized in Fig. 2, but employed two distinct sets of initial random conditions: perturbation set 2 (first column), and perturbation set 3 (second column).

$$L = \frac{1}{L_0}\int_S \sqrt{\left(\frac{\partial c}{\partial x}\right)^2 + \left(\frac{\partial c}{\partial y}\right)^2}\, dxdy, \tag{14}$$

where S is the entire computational domain, and L_0 is the initial interfacial length. Figure 4 plots the dimensionless interfacial length L as a function of the dimensionless injecting area A/π for the constant injection case (solid curves) and variant injection situation (dashed curves). This is done for the three sets of initial perturbations considered in Figs. 2 and 3. First, as expected, we notice that the solid curves stand above the dashed ones, indicating more fingering and interfacial irregularities for the constant injection case. Moreover, note that the dashed curves almost overlap, while the solids curves are not as close to each other. This indicates that the controlling mechanism via variant injection is quite insensitive to modifications in the initial conditions.

III. LIFTING MISCIBLE HELE-SHAW FLOW

A. Governing equations

The geometry of the time-dependent gap Hele-Shaw cell is sketched in Fig. 5. Consider a Hele-Shaw cell of a variable gap width $h(t)$ containing two miscible, incompressible, viscous fluids. For this lifting setup, the upper plate of the cell is elevated along the direction perpendicular to the cell plates,

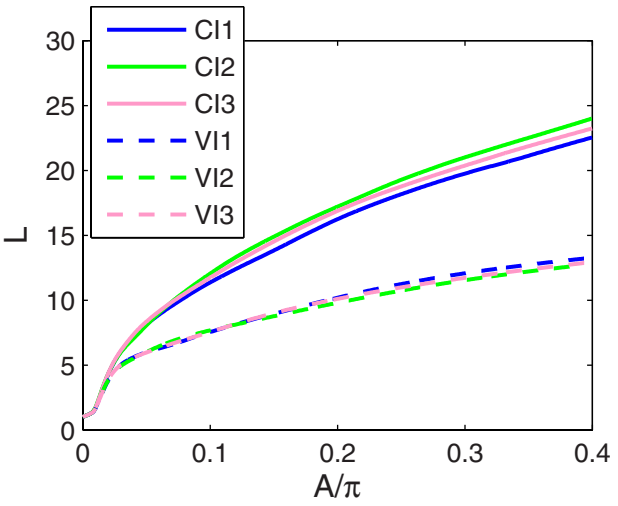

FIG. 4. (Color online) Interfacial length L as a function of the dimensionless injecting area A/π for the constant injection (CI) case, and three different sets of initial perturbations (solid curves). The dashed curves represent similar sets of data for the variant injection (VI) situation. In the inset the numbers label the different perturbation sets.

while the lower plate is held fixed. The initial plate spacing $h(t=0)=h_0$, and the initial fluid-fluid diffusive interface is circular, having radius $R(t=0)=R_0$.

As in Refs. [12,14] we assume an exponentially increasing gap width $h(t)=h_0\exp(\gamma t)$ for the conventional lifting situation, where γ is a control parameter. Here the gap averaged Hele-Shaw dimensionless expressions are a bit different from those presented in the injection-driven case [Eqs. (1)–(3)] due to the time variation of the cell gap spacing

$$\nabla\cdot\mathbf{u}=-1, \tag{15}$$

$$\nabla p=-\frac{\eta}{e^{2t}}\mathbf{u}, \tag{16}$$

$$\frac{\partial c}{\partial t}+\mathbf{u}\cdot\nabla c=\frac{1}{\mathrm{Pe}}\nabla^2 c, \tag{17}$$

where $\eta(c)=\exp[\mathcal{R}(1-c)]$, and

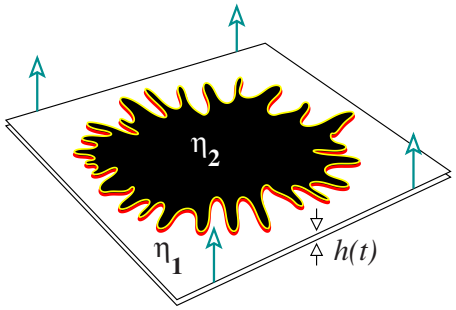

FIG. 5. (Color online) Sketch of the time-dependent gap radial Hele-Shaw flow with miscible fluids. The upper cell place is lifted, so that the cell variable gap width $h=h(t)$. The inner fluid is more viscous ($\eta_2>\eta_1$).

$$\mathrm{Pe}=\frac{\gamma R_0^2}{D} \tag{18}$$

defines a Péclet number for the lifting flow situation. Equations (15)–(17) have been made dimensionless by using R_0 as a characteristic length scale. We further scale the viscosity with η_1 and time with $1/\gamma$. Finally, velocity is rescaled by γR_0, and pressure by $(12\eta_1\gamma R_0^2)/h_0^2$.

The velocity is split into a divergence free component $\mathbf{u}_f$ which is the rotational velocity of the constant gap spacing case, and an axisymmetric divergent radial, potential velocity $\mathbf{u}_d=\mathbf{u}_d(r)$ caused by the gap variation, so that

$$\mathbf{u}=\mathbf{u}_f+\mathbf{u}_d, \tag{19}$$

$$\nabla\cdot\mathbf{u}_f=0, \tag{20}$$

$$\nabla\cdot\mathbf{u}_d=-1. \tag{21}$$

Note that the divergence free component can be obtained by solving Eq. (6) in which u_r should be replaced by u_f. The divergent radial velocity is obtained directly as $\mathbf{u}_d=-r\hat{\mathbf{r}}/2$, which is a potential field. Similarly to the injection-driven case, the divergence free component $\mathbf{u}_f$ can be obtained by solving Eqs. (6) and (7).

Following Ref. [20] for the variant dimensional lifting situation we consider that

$$h(t)=\frac{h_0}{(1-\delta t)^{2/7}}, \tag{22}$$

where δ is a control parameter with an inverse dimension of time. We utilize the same set of characteristic scales used in the exponential lifting situation to obtain the corresponding governing equations for the variant lifting case. In this context, the dimensionless continuity equation takes the form

$$\nabla\cdot\mathbf{u}=-\frac{2a}{7(1-at)}, \tag{23}$$

but Eqs. (16) and (17) remain unchanged. Note the definition of an additional dimensionless parameter, namely the lifting ratio $a=\delta/\gamma$. Likewise, in dealing with the variant lifting situation, Eqs. (19) and (20) are unaltered, but Eq. (21) is replaced by

$$\nabla\cdot\mathbf{u}_d=-\frac{2a}{7(1-at)}. \tag{24}$$

The divergent radial velocity is obtained directly as $\mathbf{u}_d=-ar\hat{\mathbf{r}}/[7(1-at)]$, which is a potential field.

B. Exponential and variant lifting scenarios: Numerical results

Here we turn to the numerical results comparing the resulting patterns under exponential lifting with those with variant lifting. As in Sec. II B we compare the fingering patterns under the same dimensional lifting effectiveness, i.e., we contrast the situations in which the patterns for exponential and variant lifting have reached an equal gap width at equal times: $h_{exp}=h_v=h$. In the following simulations, we

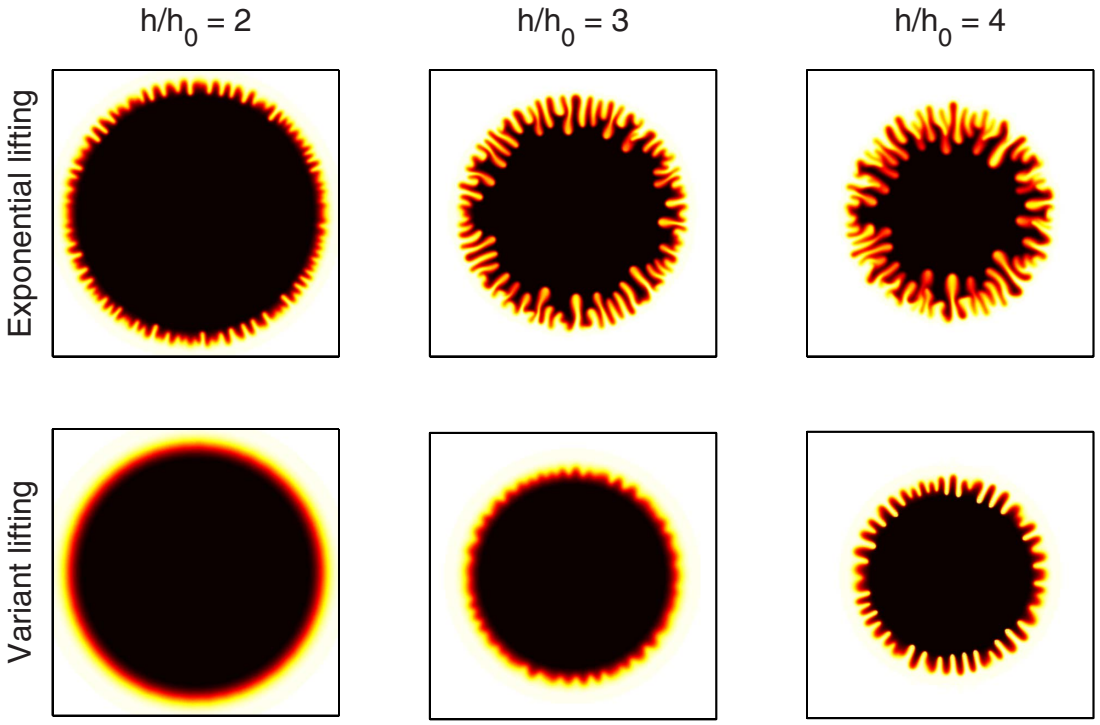

FIG. 6. (Color online) Concentration images for the dimensionless gap distances $h/h_0=2$, 3, and 4, for the cases of exponential lifting (top row), and variant lifting (bottom row).

consider characteristic values for the lifting Péclet number Pe=3000, and viscosity contrast $\mathcal{A}=0.925$. In addition we take $a=1/3$. In order to ensure the appropriateness of the Hele-Shaw approach [14], only situations of relatively small gap spacing, namely $h=2h_0, 3h_0$ and $4h_0$ are considered. For both lifting cases the boundary conditions are prescribed as

$$x = \pm 4/3: \phi = 0, \frac{\partial c}{\partial x} = 0, \tag{25}$$

$$y = \pm 4/3: \phi = 0, \frac{\partial c}{\partial y} = 0. \tag{26}$$

Figure 6 illustrates the concentration images obtained for increasingly larger values of the dimensionless gap width $h/h_0=2$, 3, and 4, both for the exponential (top row) and variant (bottom row) lifting cases. This is done for a given set initial random perturbations (perturbation set 1). During exponential lifting with $h/h_0=2$ we see the development of a large number of small fingers of the less viscous fluid penetrating the more viscous one. At $h/h_0=3$ fingering is considerably stronger where invading inward moving fingers compete more intensively giving rise to a deformed diffusive interface. Finally, for $h/h_0=4$ the patterns are even more ramified, revealing plenty of finger competition (length variability) among less viscous fingers, resulting in convoluted structures presenting forms which resemble forks and tridents. On the other hand, variant lifting reveals a quite different set of morphologies. When $h/h_0=2$ the boundary of the droplet is nearly circular, so that fingers are absent. Very mild fingering formation is then observed for $h/h_0=2$. Finally, if $h/h_0=4$ fingers emerge (about 40 or so), but in a more orderly fashion, so that finger competition among inward moving fingers is substantially suppressed. This points to the stabilizing nature of the variant lifting process. We have performed simulations for several other values of the Péclet number in the interval $2500 \leq \mathrm{Pe} \leq 3500$, and identified the very same stabilizing behavior. Despite this variation in the values of Pe we found a relatively small modification in the number of resulting fingers: for example, when $h/h_0=4$ the number of fingers changes only from 38 to 42. This supports the suitability of the controlling mechanism provided by the variant lifting in spite of sizable modifications in the Péclet number.

Similarly to what we have done in Sec. II B, we examine the response of the patterns to modifications in the initial conditions. This issue is addressed in Fig. 7 which depicts patterns at $h/h_0=4$ for both types of lifting, and two additional collections of initial conditions: perturbation set 2 (first column) and perturbation set 3 (second column). It is clear that the structures obtained in Fig. 7 are not that different from those obtain in Fig. 6 for $h/h_0=4$. However, it is worth pointing out that under variant lifting the final number of fingers practically does not change (it varies only from 41 to 43) if initial conditions are altered. A more quantitative account about this result is shown in Fig. 8 which describes the behavior of the dimensionless interfacial length L in terms of h/h_0 for exponential lifting EL (solid curves) and variant lifting VL (dashed curves). This is done for the three sets of initial perturbations considered in Figs. 6 and 7. Note the collapse of the dashed curves, a fact that reinforces the indifference of the variant lifting protocol with regards to changes in initial conditions. The strong stabilization role of the variant lifting is also evident (dashed curves located far below the solid ones).

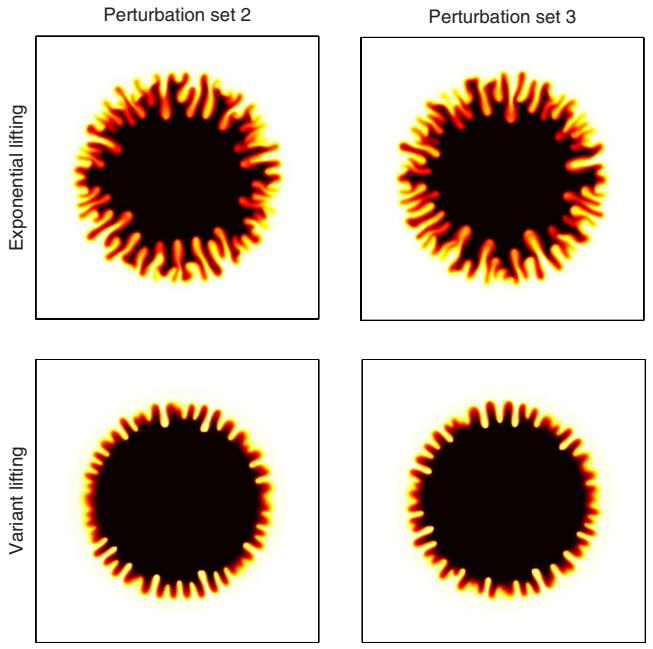

FIG. 7. (Color online) Concentration images for the dimensionless gap distance $h/h_0=4$ for the cases of exponential lifting (top row), and variant lifting (bottom row). These simulations used the same physical parameters used in Fig. 6, but utilized two distinct set of initial random conditions: perturbation set 2 (first column), and perturbation set 3 (second column).

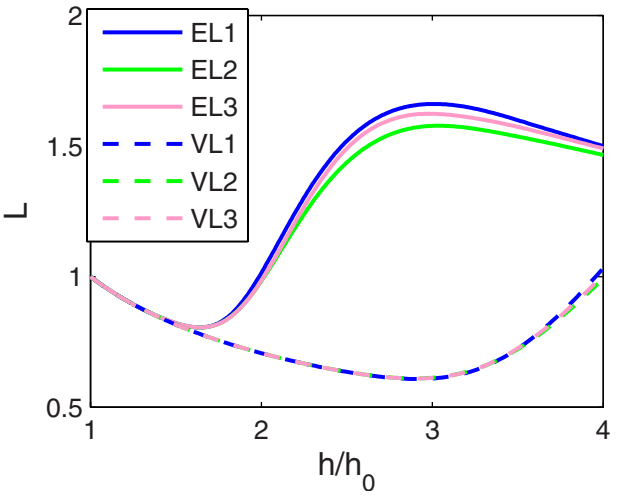

FIG. 8. (Color online) Interfacial length L as a function of the dimensionless gap distance h/h_0 for the exponential lifting (EL) case, and three different sets of initial perturbations (solid curves). The dashed curves represent similar sets of data for the variant lifting (VL) situation. In the inset the numbers label the distinct perturbation sets.

IV. CONCLUSION

Usual immiscible flows in radial Hele-Shaw geometry under constant injection rate, and exponentially varying time-dependent gap width lead to the formation of complex morphological structures. However, by properly controlling injection and lifting rates the rising of such complicated patterns can be inhibited, and replaced by much more symmetric shapes [18–20]. Nevertheless, the feasibility of these suggestive and useful procedures to miscible fluid displacements remained an open question.

We have investigated the application of these control strategies for the very same flow setups, but considering that the fluids involved are miscible. Despite the absence of surface tension effects, our fully nonlinear numerical simulations support the effectiveness of the control protocols in restraining the emergence of intricate miscible morphologies. But, in contrast to the immiscible (finite surface tension) cases, one cannot exactly prescribe the final number of fingers. However, we have found that the ultimate number of fingers is not significantly modified despite considerable changes in Péclet numbers. Moreover, we have verified that the controlling procedure is quite insensitive to changes in initial conditions.

Our results point to the robustness and efficiency of the suggested stabilizing mechanisms, even under miscible flow circumstances. Considering that controlling the development of complicated diffusive interfacial shapes is a serious challenge for a number technological applications (for instance, oil recovery [16], and adhesion science [17]), and academic research areas in physics, chemistry [30] and biology [31], we hope experimentalists will feel motivated to check, and hopefully validate the ideas put forward in this work.

ACKNOWLEDGMENTS

J.A.M. thanks CNPq (Brazilian Research Council) for financial support of this research through the program "Instituto Nacional de Ciência e Tecnologia de Fluidos Complexos (INCT-FCx)," and also through the CNPq/FAPESQ Pronex program. C.-Y. C. thanks the National Science Council of the Republic of China for financial support through Grant No. NSC 96-2221-E-009-244-MY3.

[1] P. G. Saffman and G. I. Taylor, Proc. R. Soc. London, Ser. A **245**, 312 (1958).
[2] G. Homsy, Annu. Rev. Fluid Mech. **19**, 271 (1987); K. V. McCloud and J. V. Maher, Phys. Rep. **260**, 139 (1995); J. Casademunt, Chaos **14**, 809 (2004).
[3] L. Paterson, J. Fluid Mech. **113**, 513 (1981).
[4] J.-D. Chen, J. Fluid Mech. **201**, 223 (1989); Exp. Fluids **5**, 363 (1987).
[5] H. Thomé, M. Rabaud, V. Hakim, and Y. Couder, Phys. Fluids **A1**, 224 (1989).
[6] O. Praud and H. L. Swinney, Phys. Rev. E **72**, 011406 (2005).
[7] J. A. Miranda and M. Widom, Physica D **120**, 315 (1998).
[8] P. Fast and M. J. Shelley, J. Comput. Phys. **212**, 1 (2006).
[9] J. Mathiesen, I. Procaccia, H. L. Swinney, and M. Thrasher, EPL **76**, 257 (2006).
[10] S. W. Li, J. S. Lowengrub, and P. H. Leo, J. Comput. Phys.

225, 554 (2007).
[11] C.-Y. Chen, C.-W. Huang, H. Gadêlha, and J. A. Miranda, Phys. Rev. E **78**, 016306 (2008).
[12] M. J. Shelley, F.-R. Tian, and K. Wlodarski, Nonlinearity **10**, 1471 (1997).
[13] D. Derks, A. Lindner, C. Creton, and D. Bonn, J. Appl. Phys. **93**, 1557 (2003).
[14] C.-Y. Chen, C.-H. Chen, and J. A. Miranda, Phys. Rev. E **71**, 056304 (2005).
[15] A. Lindner, D. Derks, and M. J. Shelley, Phys. Fluids **17**, 072107 (2005).
[16] S. B. Gorell and G. M. Homsy, SIAM J. Appl. Math. **43**, 79 (1983).
[17] D. J. Yarusso, in *Adhesion Science and Engineering— The Mechanics of Adhesion*, edited by D. A. Dillard and A. V. Pocius (Elsevier, Amsterdam, 2002).
[18] S. W. Li, J. S. Lowengrub, J. Fontana, and P. Palffy-Muhoray, Phys. Rev. Lett. **102**, 174501 (2009).
[19] A. Leshchiner, M. Thrasher, M. B. Mineev-Weinstein, and H. L. Swinney, Phys. Rev. E **81**, 016206 (2010).
[20] E. O. Dias and J. A. Miranda, Phys. Rev. E **81**, 016312 (2010).
[21] C. -T. Tan and G. M. Homsy, Phys. Fluids **31**, 1330 (1988).
[22] C.-Y. Chen and E. Meiburg, J. Fluid Mech. **326**, 57 (1996).
[23] C.-Y. Chen and E. Meiburg, J. Fluid Mech. **371**, 233 (1998); **371**, 269 (1998).
[24] P. Petitjeans and T. Maxworthy, J. Fluid Mech. **326**, 37 (1996).
[25] P. Petitjeans, C.-Y. Chen, E. Meiburg, and T. Maxworthy, Phys. Fluids **11**, 1705 (1999).
[26] J. Kuang, T. Maxworthy, and P. Petitjeans, Eur. J. Mech. B/Fluids **22**, 271 (2003).
[27] D. Gottlieb and S. A. Orzag, *Numerical Analysis of Spectral Methods* (SIAM, Philadelphia, 1977).
[28] C. Canuto, M. Y. Hussaini, A. Quarteroni, and T. A. Zang, *Spectral Methods in Fluid Mechanics* (Springer, Berlin, 1988).
[29] E. Meiburg and C.-Y. Chen, SPE J. **5**, 129 (2000).
[30] C. Almarcha, P. M. J. Trevelyan, P. Grosfils, and A. De Wit, Phys. Rev. Lett. **104**, 044501 (2010).
[31] A. Goriely and M. Tabor, Phys. Rev. Lett. **90**, 108101 (2003).